Coastal Engineering 173 (2022) 104097

Contents lists available at ScienceDirect

Coastal Engineering

journal homepage: www.elsevier.com/locate/coastaleng

Experimental analysis and numerical simulation of wave overtopping on a fixed vertical cylinder under regular waves

G.A. Esteban [a,*], A. Aristondo [b], U. Izquierdo [a], J.M. Blanco [a], G. Pérez-Morán [b]

[a] Energy Engineering Department, UPV/EHU, Pza. Ingeniero Torres Quevedo 1, E-48013, Bilbao, Spain
[b] Energy, Climate and Urban Transition, TECNALIA, C/ Geldo, Ed. 700, E-48160, Derio, Spain

ARTICLE INFO

Keywords:
Wave overtopping
Cylindrical structure
Physical model tests
Numerical model tests
RANS-VOF

ABSTRACT

Wave overtopping phenomenon affects relatively narrow offshore marine structures different from shoreline linear structures, where there is not defined a precise prediction methodology as it is the case of the behaviour at long coastal defences. In the present study a combined experimental and numerical approach has been followed to obtain an empirical relation that represents the relative overtopping discharge over a fixed vertical cylinder exposed to non-impulsive wave conditions. The phenomenon follows a Weibull type dependence on the relative freeboard in a similar way as the case of vertical walls but reporting a decreasing overtopping rate at higher freeboards. In addition, a direct linear relationship between the relative mean flow thickness computed at the centre of the circular crest of the cylinder and the relative overtopping discharge has been observed. This methodology may be used as an indirect cost-effective method to characterize experimentally the wave overtopping phenomenon in cylindrical structures of full-scale prototypes without the need of accumulating and characterising huge amounts of overtopped water volumes. The present study contains a systematic analysis of the dispersion obtained in the experimental and computational results to evaluate the performance attributed to the proposed empirical expressions.

1. Introduction

Wave overtopping is a very well-known phenomenon characteristic of extreme sea states where waves run-up the seawards exposed face of a structure, reach its crest and pass over it. This physical process affects a wide range of marine structures exposed to incoming waves including shoreline defence structures, fixed and floating offshore platforms (e. g. oil and gas exploitation or offshore windfarms) and breakwaters, or technological devices extracting energy from the overtopped volume (a technological alternative of a wave energy converter – WEC -). This is the reason why a great international effort has been made in last decades in ocean engineering to describe and predict the mean wave overtopping discharges and volumes over different structures corresponding to different wave characteristics. The extensive international work includes the preparation of manuals characterising the phenomenon and collaborative research projects with experimental testing and study of databases by means of trained neural network tools; e. g. CLASH database (van der Meer et al., 2009; van Gent et al., 2007). EurOtop 2018 (van der Meer et al., 2018) is a reference document collecting numerous contributions and establishing the guidelines for engineering design of coastal structures. Historically, the majority of the work published in the field focuses on shoreline sea defences as dikes, seawalls, armoured rubble slopes and mounds, and vertical, battered or steep walls, designed to prevent flooding and coastal erosion or guarantee ship protection in ports and harbours. These structures present a long 2D frontage interacting with the incoming wave front.

The usual alternatives of study are experimental tests of physical scaled models and numerical simulations of computational models in experimental or numerical wave flumes (Izquierdo et al., 2019). A brief review of the recent progress in both fields is presented as a guiding reference hereafter.

The standard experimental setup for overtopping studies consists of a wave generation system, a wave detection system, the scaled model of the structure to be analysed and a system to collect and measure the overtopped water volume. Many examples of experimental models for overtopping analysis can be found in the literature (Akgul and Kabdasli, 2017; Chen et al., 2015; Liu et al., 2018; Nørgaard et al., 2014; Pearson et al., 2001; Pillai et al., 2017; Tuan et al., 2006; Vázquez et al., 2016; Victor et al., 2012; Williams et al., 2019; Zeidler et al., 1994). The wave generation system usually consists of a piston that moves a paddle,

* Corresponding author.
E-mail address: gustavo.esteban@ehu.eus (G.A. Esteban).

https://doi.org/10.1016/j.coastaleng.2022.104097
Received 12 July 2021; Received in revised form 17 December 2021; Accepted 1 February 2022
Available online 3 February 2022

generating regular or irregular waves. While regular waves show the same amplitude and period, irregular waves contain random values following a certain spectrum; i. e. an occurrence density function. Popular wave spectra are the Pierson-Moskowitz spectrum (Pierson and Moskowitz, 1964) and the JONSWAP spectrum (Hasselmann et al., 1973), which is a generalized form of the Pierson Moskowitz spectrum, considering a peak enhancement factor. Another important feature of wave generation is the option of installing an active absorption system of reflected waves. The lack of an active absorption system limits the duration of each test to the time taken by the reflected waves to travel from the testing structure to the reciprocating paddle and back to the structure (Chen et al., 2015). Measurement of incident wave characteristics is usually done by means of resistive-type wave probes, which are located along the flume. These are used to obtain the time series data of free surface elevation from which incident wave heights, periods and wavelengths are obtained. Free surface elevation time series are also used to separate the incident and reflected wave spectra (Mansard and Funke, 1980), and (Isaacson, 1991).

In order to measure and quantify the mean overtopping discharge and the overtopping volumes, the typical setup consists of a calibrated tank located behind the structure that collects the water that has overtopped the structure. Usually, a chute is used to direct the overtopped water to the calibrated tank. Two main techniques are used to determine the overtopped volume in the tank: level gauges and weight or load cells. The former consists of a typical resistive wave gauge placed in the tank measuring the time series of water level increase in the calibrated container. The mean overtopping discharge is calculated from the filling time and the water level variation measured in the tank (Nørgaard et al., 2014; Pillai et al., 2017; Williams et al., 2019). The second method consists of installing load cells, weight cells or depth-type pressure gauges in order to measure the mass of liquid accumulated in the tank (Liu et al., 2018; Victor et al., 2012).

On the other hand, numerical simulation can be used to study the overtopping phenomenon in a flexible way without restrictions coming from geometric constraints. This approach consists of solving numerically the conservation laws of fluid motion (i. e. mass and momentum) in the computational flow field to represent the behaviour of the waves interacting with solid structures where run-up and overtopping processes may occur. Two main alternatives are used: (1) The Eulerian approach, where pressure and the three flow field velocity components are calculated by solving numerically in a discretized space the continuity equation and the Reynolds Averaged Navier Stokes (RANS) to the mean flow characteristics. In this case, the use of the technique of the Volume of Fluid (VOF equations together with some turbulence model that infer the effect of pulsating variable components associated) (Hirt and Nichols, 1981) is common practice to treat the motion of the free surface. VOF calculates the so-called volume fraction field function to represent the volumetric fraction of each phase (liquid or gas) that is present at each cell of the computational domain and, in this way, it allows for free surface computation and tracking. (2) The Lagrangian approach of Smooth Particle Hydrodynamics (SPH), where the same physical properties of the fluid are calculated for fluid particles or blobs in a mesh-free computational domain, instead of space points, by again computing the mass conservation and momentum balance laws for each fluid element that is related with the neighbor elements through a certain kernel smoothing function (Dalrymple et al., 2002).

Eulerian approach has been extensively used for the study of fixed structures as breakwaters, dikes or dams (Buccino et al., 2019a, 2019b; Lu et al., 2007; Zhang et al., 2019; Chen et al., 2021; Liu et al., 2021), including benchmark work to assess the performance of different CFD alternatives (Lashley et al., 2020). In addition, this VOF-RANS approach has been applied to simulate the extraction of energy from overtopped volumes in breakwaters (Contestabile et al., 2020; Di Lauro et al., 2019, 2020; Han et al., 2018; Musa et al., 2017), the CFD models being validated by comparison with flume experimental tests. In addition, the Lagrangian SPH approach has been applied successfully to the study of overtopping on different seawalls and decks (Dang et al., 2021; Gómez-Gesteira et al., 2005; Shao et al., 2006; Vanneste et al., 2014).

All this profound work leads to a very well definition of the problem in long linear structures interacting with overtopping waves. However, other different constructions are also used in technology fields of ocean engineering like in offshore renewable energy (ORE) where individual devices with relatively narrow dimensions in comparison to the longitudinal scale of the impinging wave front are used. For instance, a simple cylindrical geometry can be observed in a fixed monopile foundation of a wind turbine, a spar buoy with a transition to the tower of an offshore floating wind turbine (FOWT) or cylindrical active ballast tanks of submersible wind platforms. In all these cylindrical structures emerging from the sea with a horizontal boundary as its crest, either the total circular base of the cylinder or an annular transition piece, overtopping is worth being studied and predicted because it may imply a damaging water impact hazard on the infrastructures, facilities and equipment mounted on the overtopped volume affected spaces (including breaching of structures and or flooding of internal chambers) or just a modification of the hydrodynamic behaviour of a certain design when interacting with the waves. The severity of the phenomenon can be classified in terms of the predicted overtopping discharge, q, together with the wave height (typically the significant wave height H_{m0}).

To the knowledge of the authors, there is no reference to any experimental, numerical or analytical description of the overtopping phenomenon over a cylindrical geometry. In principle, the result of the interaction of a wave front with a narrow cylinder is different from the case of a 2D long structure because of lateral effects along the sway direction.

In this piece of research a combined computational and experimental study has been performed in search of a specific empirical correlation that predicts the overtopping discharge on a fixed vertical cylinder, valid for a wide range of monochromatic non-impulsive waves. A broad experimental campaign has been performed with a scaled physical mock-up to validate a VOF-RANS based CFD model capable of characterising the wave overtopping phenomenon without the inconvenience of the specific measuring technique interfering the progress of the wave interaction during the overtopping process itself. Finally, as a result of the computational tests, empirical governing equations are provided for the evaluation of the mean overtopping discharge and the overtopping flow thickness as a function of the wave characteristics and geometry of the cylindrical structure.

2. Theoretical background

Wave overtopping takes place in three different ways. Green water overtopping occurs when wave run-up is high enough for the waves to pass over the crest of the structure in the form of a continuous water layer (non-impulsive regime). White water overtopping occurs when waves break on the seaward face of the structure, producing highly aerated volumes of splash that are carried over the structure (impulsive regime). Finally, a less important form of overtopping occurs as water spray produced due to the interaction between the wind and wave crests immediately offshore of the wall passes over the structure. However, even under strong wind conditions the contribution of this last form of overtopping can be neglected for engineering purposes.

Wave overtopping is affected by several parameters characteristic of the sea-state and the geometry of the structure and foreshore. Wave height (H), period (T), steepness (s) and water depth (h) at the toe of the structure are the main parameters to be considered when analysing the influence of the sea state on overtopping. Geometric parameters of the structure, such as the foreshore, slope, berm and, mainly, the crest freeboard (R_c) are also critical when studying wave overtopping.

Wave overtopping is a highly non-linear phenomenon difficult to describe by simple analytical models. The estimation of wave overtopping for a certain structure is carried out using empirical expressions obtained from numerical modelling or scaled physical model tests. Both

methods are particularly useful when assessing wave overtopping because this phenomenon is affected by different factors whose individual and combined influences are still largely unknown and difficult to predict. The empirical approach produces a simplified representation of the physics of the process, usually given as an equation relating dimensionless parameters characteristic of the phenomenon (i. e. overtopping discharge, wave parameters and geometric factors of the structure).

The widely accepted empirical model for the prediction of wave overtopping is the following Weibull-type function (van der Meer et al., 2018):

$$\frac{q}{\sqrt{gH_{m0}^3}} = a \cdot exp\left[-\left(b\frac{R_c}{H_{m0}} \right)^c \right] \quad (1)$$

where q is the mean overtopping discharge, H_{m0} is the significant spectral wave height and R_c is the crest freeboard. The mean overtopping discharge, q, is the main parameter used to describe the overtopping process accounting for the average water volume per unit time and transversal horizontal length of structure passing over. The freeboard, Rc, is the elevation difference between the structure crest and the still water level (SWL). The significant wave height, H_{m0}, is 4 times the root mean square displacement of the free surface that is equivalent to the average height of the 1/3 highest waves of a series of irregular waves. Equation (1) is a Weibull-shaped function relating the overtopping discharge to the crest freeboard, both nondimensionalized with the significant wave height to define the relative discharge and relative freeboard respectively. This expression covers the whole range of relative freeboard from higher values of zero overtopping to lower values including the case of zero freeboard. Parameters a, b and c depend on the case under study, and have to be derived from real overtopping data analysis (either physical model test data or numerical analysis data). An extensive compilation on the use of empirical models for different structure configurations can be found in EurOtop (2018) (van der Meer et al., 2018). In the particular case of this investigation, the wave height of regular waves, H, have been used instead of the significant wave coming from spectral analysis.

For the assessment of wave overtopping the wave/structure interaction regime needs to be identified, because very different responses are expected in each case. In the particular case of battered or vertical walls, which is the reference case due to its analogy with the fixed vertical cylinder, overtopping can take place under two different regimes: impulsive and non-impulsive conditions. Non-impulsive conditions occur when the height of the waves is relatively small in comparison to local depth at the structure toe and the wave steepness is low and far from the breaking limit. Under these conditions overtopping waves produce smoothly varying loads and green-water flow over the structure. On the other hand, impulsive conditions occur at vertical or steep walls when wave heights are larger in relation to local water depths and show a high wave steepness. In this case, the wave breaks against the structure producing a highly accelerated vertical jet-like water flow that jump over the structure because of inertia leading to a great amount of overtopped water volumes. In the presence of a foreshore, the likelihood of impulsive or non-impulsive overtopping is determined using the so-called "impulsiveness" parameter (van der Meer et al., 2018):

$$h^* = \frac{h^2}{H_{m0}L_{m-1,0}} \quad (2)$$

where $L_{m\text{-}1,0} = g(T_{m\text{-}1,0})^2/2\pi$ is the deep water wavelength *corresponding to the wave energy period* $T_{m\text{-}1,0}$. A high value of this discriminator $h^* > 0.23$ indicates non-impulsive conditions.

In addition to the impulsiveness, the existence of a sloping foreshore in shallow or intermediate depth water have a decisive effect on the overtopping process, because it may cause shoaling, steepening and breaking of the wave along its propagation towards the structure.

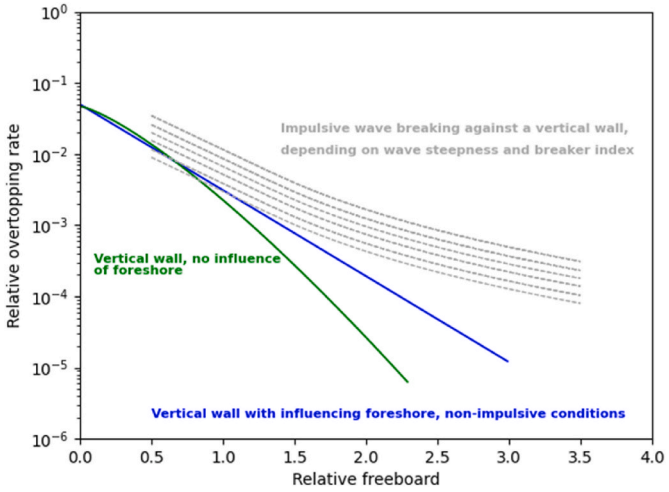

Fig. 1. Overview of the regimes of wave overtopping at vertical structures. (Higher dashed lines correspond to greater breaker index H_{m0}/h and smaller wave steepness $s_{m\text{-}1,0}$. (Fig. 13 in van der Meer and Bruce, 2014).

Fig. 1 shows a qualitative approach of the overtopping response of vertical structures subjected to impulsive regime and non-impulsive regime, with the presence of an influencing foreshore and without it.

For vertical seawalls with no influencing foreshore under non-impulsive conditions, relative overtopping rate mainly depends on the relative crest freeboard and can be estimated using the following Weibull-shaped function (3):

$$\frac{q}{\sqrt{gH_{m0}^3}} = 0.047 \cdot \exp\left[-\left(2.35\frac{R_c}{H_{m0}} \right)^{1.3} \right] \quad (3)$$

Alternative expressions are reported when there is an influencing foreshore (exponential type, $c = 1$) and for impulsive conditions (potential type) leading to higher overtopping relative discharges for the same relative freeboard. Here, equation (3) is retained as a reference because in this piece of research a fixed cylinder is submitted to non-impulsive waves without any influence of the foreshore.

An additional indirect response to the overtopping phenomenon studied here is the overtopping flow thickness δ. This parameter stands for the thickness of the water layer flowing over the crest of the structure. Here, the average flow thickness, $\bar{\delta}$, measured at the centre of the crest is calculated by averaging the time evolution of the parameter over the time period taken by the event Δt:

$$\bar{\delta} = \frac{1}{\Delta t}\int_0^{\Delta t} \delta(t)dt \quad (4)$$

The direct relationship of this parameter with the overtopping discharge and its dependence on wave characteristics and geometric factors of the structure is an additional objective of this work.

3. Aims and methodology

The main goal of this paper is to study the parametric dependence of wave overtopping over a fixed vertical cylinder, and to develop an empirical prediction model able to estimate the overtopping discharge. The particular geometry of a vertical cylinder is worth studying because it is a very common structure in the offshore wind sector that can be found in bottom-fixed sub-structures, such as monopiles and jackets, or in floating sub-structure solutions such as spar-buoys (Jonkman, 2010) and semi-submersible platforms (Galván, 2018).

Overtopping has been studied using both a physical and a numerical

Fig. 2. Experimental wave flume overall view (top). Impermeable adjustable parabolic beach (bottom-left). Resistive-type wave probes (bottom-centre). Wavemaker (bottom-right).

model. First, an experimental test campaign has been performed using a physical mock-up with the presence of a water collecting structure to measure the overtopping water volume. These experimental results have been used to validate a numerical CFD model that includes both the cylinder and the collecting structure to capture the simultaneous influence. Once the model has been validated, the same numerical configuration has been applied to analyse the overtopping phenomenon on a solitary cylinder preventing the influence of the collecting structure.

3.1. Physical model tests

3.1.1. Test facility

The experimental wave flume (Fig. 2) of the Energy Engineering Department - UPV/EHU has been used in the experimental campaign. Its dimensions are 12.5 m in length, 0.60 m in width and 0.7 m in height; it is formed by a stainless-steel base enclosed by laminated and tempered glass vertical walls. The flume is equipped with a piston-type wavemaker and a self-designed parabolic impermeable beach with adjustable sloping angle and height to minimize reflection at the end of the flume. Waves are generated by the wavemaker by using Delta-ASDA (V5) software that controls the Delta AC (ASDA-A2 series) servo drive and servomotor. The servomotor is connected to a K series linear actuator (KM60-10 roller screw model) attached to a vertical paddle acting on the total water depth. It provides a rated output power of 0.75 kW, with a maximum torque of 7.16 N m and a maximum turning speed of 5 000 rpm. The rotatory motion of the servomotor, commanded by the software, is transformed into a linear displacement of the paddle, which is the responsible of generating waves. The linear actuator shows a maximum force of 3 kN and maximum linear speed of 833 mm/s.

3.1.2. Experimental setup

The physical scaled model consists of a vertical cylinder followed by a water collecting structure to capture and measure the overtopping water volume (Fig. 3). When incoming waves overtop the cylinder, the overtopping flow enters the chute that conducts the water to a calibrated tank where it is accumulated and measured.

Waves are generated by the reciprocating motion of the wavemaker in the generation region and develop along the transition zone. Gauges R1, R2 and R3 measure the free surface displacement and characterize the incident wave pattern at a distance of 6 m from the generation zone. In addition, the wave time series measured by these wave probes allows for calculating the reflection coefficient coming from the wave interaction with the overtopping model and the parabolic extinction beach. The method of Mansard & Funke (Mansard and Funke, 1980) has been followed for this purpose.

Once the waves reach the cylinder, the overtopping flow thickness $\delta(t)$ is measured by gauge R4, which is installed with its end inside a small well drilled at the crest of the solid cylinder to guarantee a continuous signal of the water level thickness including the reading of the zero.

The overtopping volume is conducted to the calibrated tank through an inclined chute and provokes level variations captured by gauge R5, which is conveniently protected from direct water splash. The top part of the cylinder is interchangeable to allow for different total cylinder height analysis. The fraction of the waves that is not captured by the cylinder and the collecting system dissipates on the absorbing beach at the end of the flume, which is oriented to minimize wave reflection. Data acquisition is carried out using an ad-hoc LabVIEW program (National Instruments, 2018).

3.1.3. Test programme

The physical model tests have been conducted under regular wave conditions. The test matrix (Table 1) considers wave heights ranging from H = 0.09 m–0.14 m in steps of 0.01 m, and four different periods: T = 0.8 s, 0.9 s, 1.1 s and 1.3 s. These values have been established by applying Froude similitude with a reducing scale factor of 1:100 to waves of 9 m–14 m high with periods of 8 s–13 s representative of sea state extreme conditions. These wave conditions are characterized by a Beaufort number between 10 and 11 corresponding to a violent storm. The cylinder has a diameter of D = 0.11 m corresponding to a full-scale diameter of 11 m. The resulting flume width to structure width ratio is greater than 5:1, which is the common rule of thumb used to neglect the effect of lateral walls in long, narrow flumes (Chakrabarti, 1994).

Two different cylinder heights have been tested, 0.34 m and 0.39 m, with two different water depths of $h = 0.3$ m and $h = 0.32$ m for the different wave heights H of the matrix. Each test has been performed three times, showing a very good repeatability.

Considering all the parameter combinations, the experimental test campaign covers a wide range of relative crest freeboard (R_c/H) from 0.14 to 1. The breaker index, H/h, stays between 0.28 and 0.47 for all cases, meaning that waves are not depth limited, but could be affected in the presence of a gentle sloping foreshore (van der Meer and Bruce,

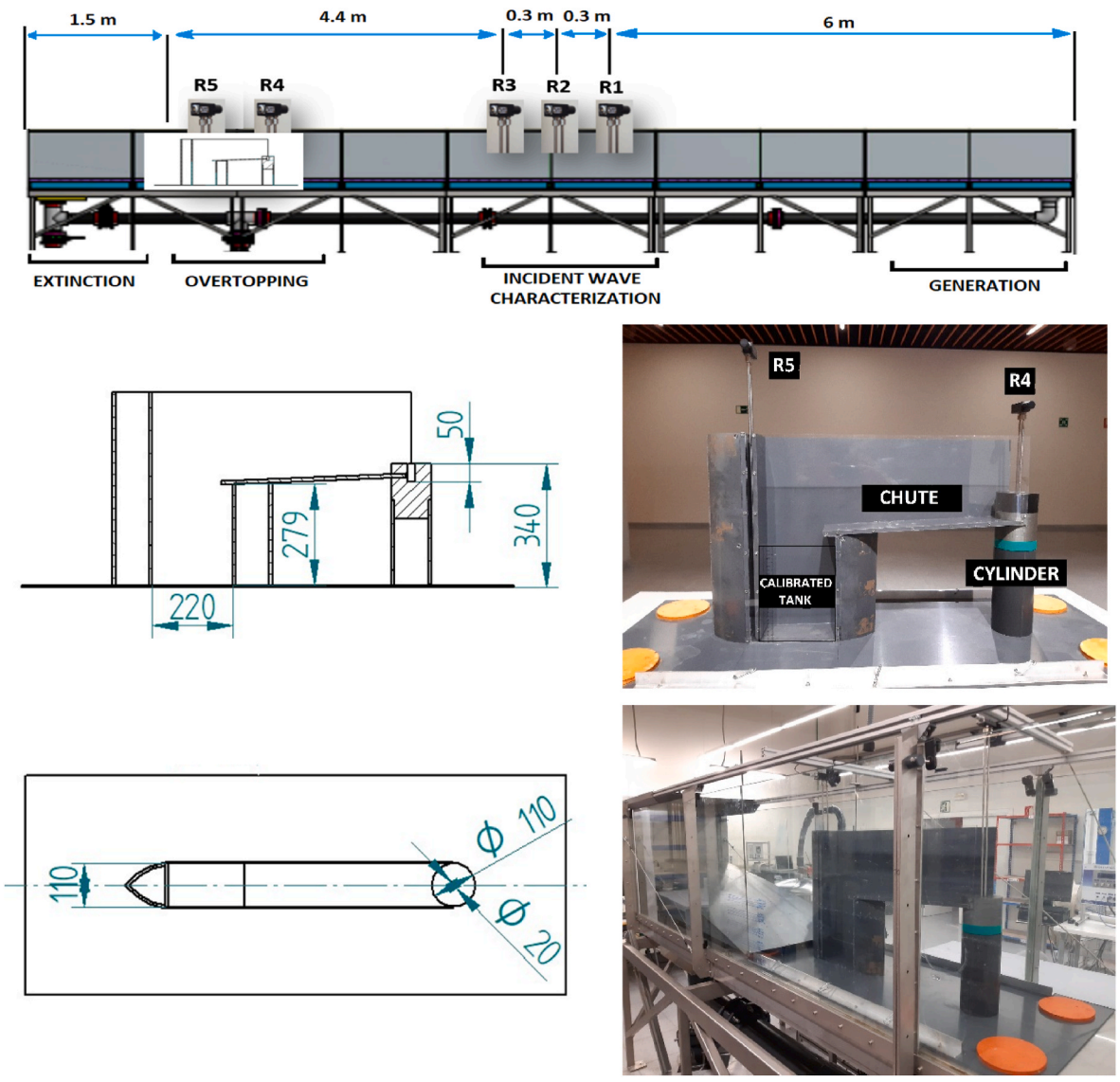

Fig. 3. Scheme of the experimental setup (top). Side view (middle-left) and top view (bottom-left) of the physical model, lengths in mm. Physical model parts (middle-right). Physical model installed in the flume (bottom-right).

Table 1
Wave test matrix.

Period: T [s]	Height: H [m]					
0.8	0.09	0.10				
0.9	0.09	0.10	0.11			
1.1	0.09	0.10	0.11	0.12		
1.3	0.09	0.10	0.11	0.12	0.13	0.14

2014). Parameter h/λ ranges between 0.15 and 0.32, which means that the experiments operate in intermediate water far from shallow water regime ($h/\lambda < 0.05$) where shoaling effects may appear more easily. The range of the impulsiveness parameter (Eq. (2)) varies from $h^* = 0.25$ to 1.14 (greater than 0.23) indicating the non-impulsive character of the overtopping process, as it has been observed qualitatively during the experimental tests.

The fact that the overtopping phenomenon is studied for non-impulsive wave conditions on a vertical structure leads to expect little influence of scale effects (Pullen et al., 2003), though the extent of such an influence would need further research with full scale prototypes.

The specific pattern applied to the time evolution of the wavemaker stroke $X_{WM}(t)$ is defined by equations (5) and (6) with a second order term characteristic of the second-order Stokes' wave theory in order to avoid unwanted free secondary waves arising when an exclusive sinusoidal motion of the paddle is applied (Hughes, 1993):

$$m_1 = \frac{H}{S} = \frac{2\,(\cosh 2\,kh - 1)}{\sinh 2\,kh + 2kh} \tag{5}$$

$$X_{WM}(t) = \frac{H}{2m_1}\sin \omega t + \frac{H^2}{32h}\left(\frac{3\cosh kh}{\sinh^3 kh} - \frac{2}{m_1}\right)\sin 2\,\omega t \tag{6}$$

where m_1 is the wave height to paddle stroke ratio H/S, $\omega = 2\pi/T$ is the wave frequency in rad/s, $k = 2\pi/\lambda$ is the wave number and h is the water depth.

Ursell number, $Ur = H\lambda^2/h^3$, accounts for the ratio of the nonlinear term of finite amplitude wave solution to the linear term of small amplitude wave solution (Ursell, 1953). Therefore, this parameter is a measure of the nonlinearity of waves. Low Ursell numbers, $Ur \ll 1$, apply to small amplitude linear wave theory. The second-order Stokes' wave theory is applicable to a range of moderately high values of Ursell number below the following threshold:

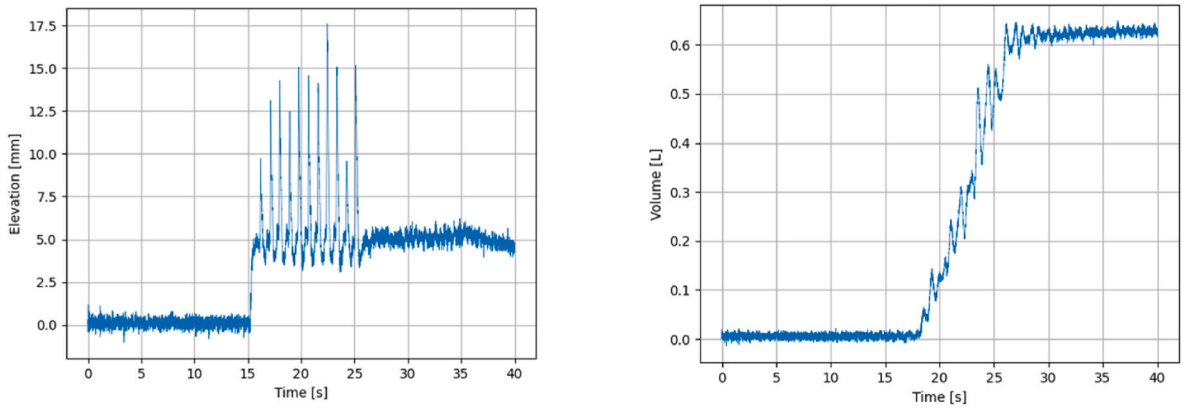

Fig. 4. Flow thickness by R4 (left). Accumulated volume by R5 (right). Test: H = 0.9 m, T = 0.9 s, h = 0.3 m, R_c = 0.04 m.

$$Ur < \frac{8\pi^2}{3} = 26 \tag{7}$$

This is the range of the validity for equations (5) and (6), which has been checked for the experimental campaign with values of Ursell number varying from 2.8 to 21.1.

Prior to the analysis of the results, the data extracted from the test campaign are post-processed in order to obtain the desired parameters. First, the wave height, period and wavelength are calculated from the wave elevation time series captured by wave probes R1, R2 and R3. Wave heights and periods are obtained by averaging individual wave values obtained by means of zero up-crossing method (Viriyakijja and Chinnarasri, 2015). For the determination of wavelength, a Fast Fourier Transform (FFT) is applied to the elevation recordings from both gauges. The phase shift between the main harmonic of both recordings ($\Delta\varphi$) is used to determine the generated wavelength. As the separation between each pair of gauges is known (Δx), wavelength can be determined using (8).

$$\lambda = 2\pi \frac{\Delta x}{\Delta \varphi} \tag{8}$$

The mean overtopping discharge $\bar{\delta}$ is computed from the instantaneous elevation data measured by R4 and the instantaneous overtopped volume is measured directly by the resistive level gauge R5 after the calibration process of the container (determination of level increase for each incremental water weight addition measured by a precision weighing scales) (Fig. 4).

The accumulated volume, V_o, is directly computed as the difference between the final and initial volume inside the tank. From this value the mean overtopping flow rate Q and the mean overtopping discharge q are calculated by considering the total overtopping time, t_o, and the diameter of the cylinder, D, (9):

$$q = \frac{Q}{D} = \frac{V_o}{t_o \cdot D} \tag{9}$$

The calculation of the mean flow thickness is performed by applying equation (4) numerically to the signal measured by gauge R4. These values will be used to find a relationship between the mean flow thickness and the associated relative overtopping discharge produced during each test.

This experimental campaign has been performed at a low reflection coefficient range of K_r between 0.01 and 0.05. This has been possible by following the methodology described in (Izquierdo et al., 2021) by accommodating the sloping angle and height of the adjustable parabolic beach depending on the characteristic of the analysed waves (depth and wave number).

3.2. Numerical model

3.2.1. Governing equations

In this section, the conservation equations that are solved numerically in the discretized flow field are presented. The first equation describing the flow motion of an incompressible fluid is the equation of the conservation of mass:

$$\frac{\partial U_i}{\partial x_i} = 0 \tag{10}$$

In addition, the equation of the conservation of momentum in the form of Reynolds Averaged Navier-Stokes (RANS) are applied in order to account for the effects of turbulence, where the velocity components are separated into mean and fluctuating components and averaged in time. This process introduces the additional Reynolds-stress tensor ($\rho\overline{u_i' u_j'}$) in the momentum equations to be modelled in terms of mean flow characteristics:

$$\frac{\partial U_i}{\partial t} + \frac{\partial (U_i U_j)}{\partial x_j} = \frac{1}{\rho} \frac{\partial}{\partial x_j} \left(-p\delta_{ij} + 2\mu S_{ij} - \rho\overline{u_i' u_j'} \right) + F_i + S_i \tag{11}$$

$$S_{ij} = \frac{1}{2} \left(\frac{\partial U_i}{\partial x_j} + \frac{\partial U_j}{\partial x_i} \right) \tag{12}$$

where $i, j = 1, 2, 3$ are the three spatial dimensions, U_i is the ith time-averaged velocity component, u'_i is the fluctuating velocity component, ρ is fluid density, S_{ij} is the viscous stress tensor (12) and δ_{ij} is the Kronecker delta function. p stands for pressure, F_i is the ith component of the external field force per unit mass (i.e. the acceleration of gravity in this particular case) and S_i represents a possible source or sink of the ith component of the momentum.

In this study, the commercial CFD software STAR CCM+ (v14.06) has been used by implementing the RANS based approach to solve the fluid flow variables and discretizing the domain according to the finite volume method. The fluctuating components of the Reynolds-stress tensor are modelled according to the Boussinesq hypothesis:

$$-\rho\overline{u_i' u_j'} = \mu_t \left(\frac{\partial U_i}{\partial x_j} + \frac{\partial U_j}{\partial x_i} \right) - \frac{2}{3} \left(\rho k_t + \mu_t \frac{\partial U_i}{\partial x_i} \right) \delta_{ij} \tag{13}$$

where k_t is the turbulent kinetic energy and μ_t is the eddy viscosity. In the present work, the Standard Low-Re k-ε model is used to model the turbulence. This model introduces two additional transport equations; one for the turbulent kinetic energy, k_t, (14) and another for the turbulent kinetic energy dissipation rate, ε_t (15). The eddy viscosity, μ_t, can be expressed as a function of the turbulent kinetic energy, k_t, and the turbulent dissipation rate, ε_t (16).

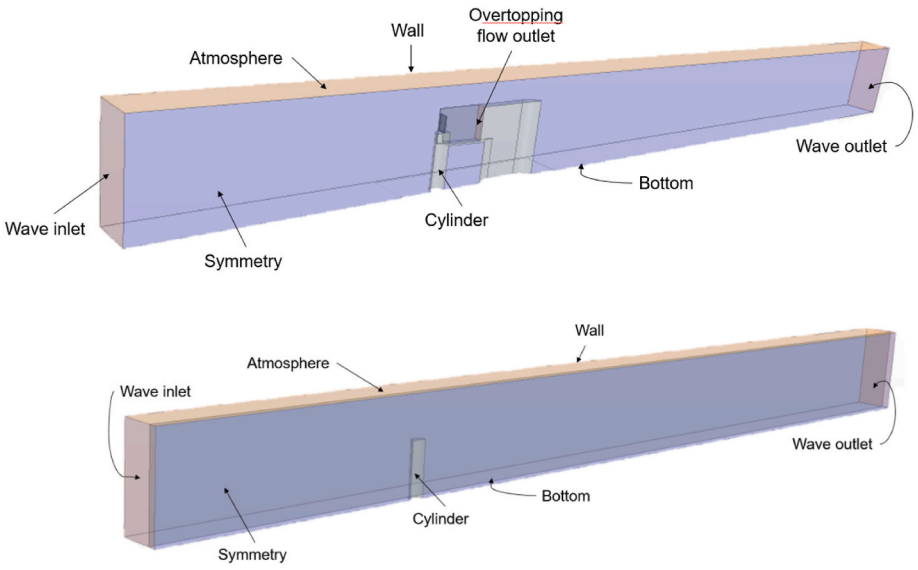

Fig. 5. Computational domain including the collecting structure (top) and with the cylinder only (bottom).

$$\rho\frac{\partial k_t}{\partial t}+\rho U_j\frac{\partial k_t}{\partial x_j}=s_{ij}\frac{\partial U_i}{\partial x_j}-\rho\varepsilon_t+\frac{\partial}{\partial x_j}\left[\left(\mu+\frac{\mu_t}{\sigma_k}\right)\frac{\partial k_t}{\partial x_j}\right] \tag{14}$$

$$\rho\frac{\partial \varepsilon_t}{\partial t}+\rho U_j\frac{\partial \varepsilon_t}{\partial x_j}=C_{\varepsilon_1}\frac{\varepsilon_t}{k_t}+s_{ij}\frac{\partial U_i}{\partial x_j}-C_{\varepsilon_2}\rho\frac{\varepsilon_t^2}{k_t}+\frac{\partial}{\partial x_j}\left[\left(\mu+\frac{\mu_t}{\sigma_\varepsilon}\right)\frac{\partial \varepsilon_t}{\partial x_j}\right] \tag{15}$$

$$\mu_t=\frac{\rho C_\mu k_t^2}{\varepsilon_t} \tag{16}$$

where the following empirical closure coefficients are used (Launder and Sharma, 1974): $C_{\varepsilon 1}=1.44$, $C_{\varepsilon 2}=1.92$, $C_\mu=0.09$, $\sigma_k=1.0$ and $\sigma_\varepsilon=1.3$.

In the numerical model the two different phases of air and water are modelled by the VOF approach, allowing for the interface capture and tracking. This method calculates the volume fraction of each fluid (air and water) at each computational cell and, as a result, it detects the position of the free surface as an abrupt change in the value of the parameter. The conservation of the individual phases is stated by the following equation:

$$\frac{\partial \alpha}{\partial t}+\nabla\cdot\left(\alpha\vec{U}\right)=0 \tag{17}$$

where α represents the water volume fraction. The properties of density and dynamic viscosity in a computational cell with a mixture of the two phases is computed from the volume fraction α as follows:

$$\rho=\alpha\rho_{water}+(1-\alpha)\rho_{air} \tag{18}$$

$$\mu=\alpha\mu_{water}+(1-\alpha)\mu_{air} \tag{19}$$

3.2.2. Computational domain and boundary conditions

The computational domain has been defined to reproduce the conditions of the experimental tests. Two different simulation setups have been used (Fig. 5). First, during the validation stage of the numerical model, the whole overtopping device (Fig. 5-top) has been introduced in the simulations, considering both the cylinder and the water collecting structure. After the validation process, the cylinder alone has been considered in order to eliminate the effect of the collecting structure on the wave-cylinder interaction (Fig. 5-bottom).

In the numerical models, the wave generation and dissipation have been implemented numerically at the corresponding boundaries to reduce the computational cost.

In the position of the wave generation system a wave inlet boundary has been defined, where high order Stokes waves are generated by means of the free surface elevation (20), velocity potential (21) and pressure field (22) by particularising the equations developed by (Fenton, 1985) for $x=0$:

$$\eta(x,t)=h+\frac{1}{k}\left(\varepsilon\cos k(x-ct)+\varepsilon^2 B_{22}\cos 2k(x-ct)+\varepsilon^3 B_{31}(\cos k(x-ct)-\cos 3k(x-ct))+\varepsilon^4(B_{42}\cos 2k(x-ct)+B_{44}\cos 4k(x-ct))\right.$$
$$\left.+\varepsilon^5(-(B_{53}+B_{55})\cos k(x-ct)++B_{53}\cos 3k(x-ct)+B_{55}\cos 5k(x-ct))\right) \tag{20}$$

Table 2
Damping parameters.

$f_1=\frac{2\pi^2}{T}$	$f_2=0$	$n_d=0$	$x_{ed}-x_{sd}=2\lambda$

$$\varnothing(x,z,t)=(c-\overline{u})x+C_0\left(\frac{g}{k^3}\right)^{\frac{1}{2}}\sum_{i=1}^{5}\varepsilon^i\sum_{j=1}^{i}A_{ij}\cosh jkz\sin jk(x-ct) \tag{21}$$

$$p(x,z,t)=\rho\left(R-gz-\frac{1}{2}\left[(u-c)^2+w^2\right]\right) \tag{22}$$

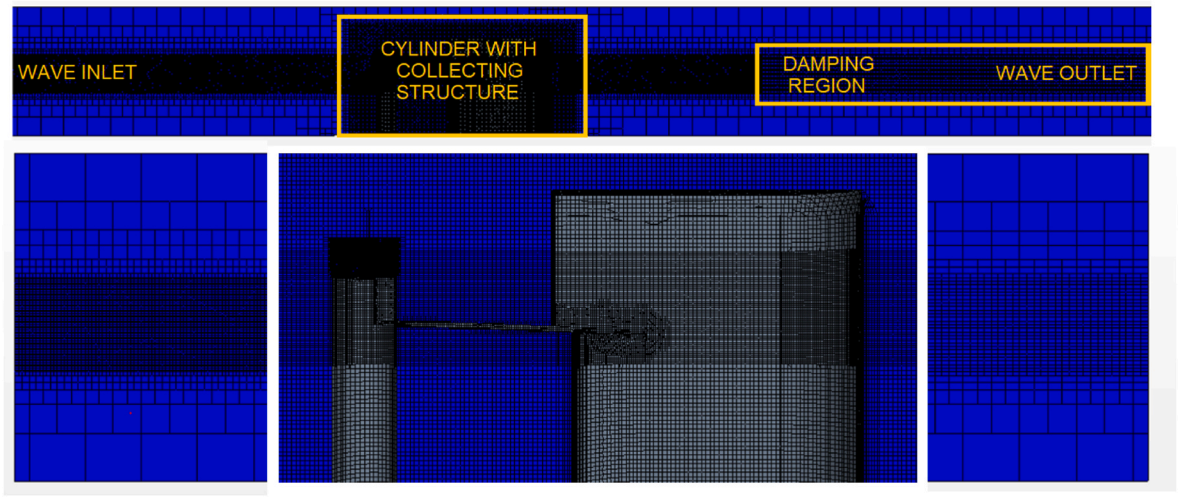

Fig. 6. Whole domain mesh (top). Local mesh refinement at the free surface (bottom-left). Local mesh refinement at the cylinder (bottom-centre). Local mesh refinement at the damping region (bottom-right).

where h is water depth, k is the wave number, c is wave celerity, $\varepsilon = kH/2$, H being the wave height. x is the position in the advancing direction of the waves, z is the vertical position and u and w are the horizontal and vertical fluid particle velocities, defined as the derivative of the velocity potential with respect to the corresponding spatial direction. The values of the parameters R, A_{ij}, B_{ij}, C_0, $\overline{u}$ can be found in (Fenton, 1985). At the wave inlet section of the domain, the fluid velocity in the vertical and the wave propagation direction is imposed according to the spatial derivatives of the velocity potential (21).

At the wave outlet section of the domain, the theoretical hydrostatic pressure of the fluid is imposed. In addition, a damping region is defined along the upstream region from this boundary in order to avoid the wave reflection. For such damping region, a resistance term is added (equation (23) and (24)) in the momentum equation (11) to reduce progressively the value of the vertical velocity w (Choi and Yoon, 2009):

$$S_z^d = \rho(f_1 + f_2|w|)\cdot\frac{e^{\kappa}-1}{e-1}w \tag{23}$$

$$\kappa = \left(\frac{x - x_{sd}}{x_{ed} - x_{sd}}\right)^{n_d} \tag{24}$$

where x_{sd} and x_{ed} are the starting and ending (boundary) points of the damping region, f_1, f_2 and n_d are parameters of the damping model. The extensive work carried out by (Perić and Abdel-Maksoud, 2016) has been used in order to optimally set up the damping parameters for each simulation (Table 2):

Every rigid wall in the simulation (flume bottom, lateral wall and cylinder surface) has been defined as an impermeable wall with non-slip condition. The top boundary of the atmosphere has been defined as a constant pressure air outlet boundary with a pressure of 1 atm. Turbulent kinetic energy and dissipation rate have been set to $1{\cdot}10^{-5}$ J/kg and

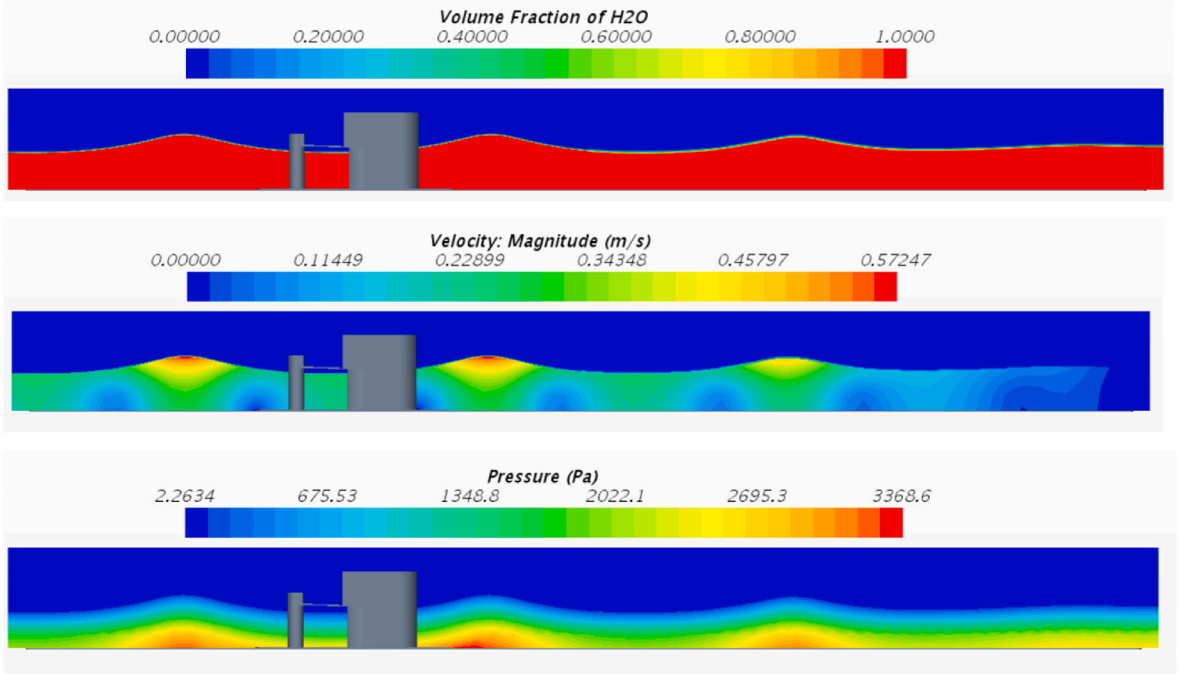

Fig. 7. Free surface initialization (top). Velocity contours at initialization (middle). Pressure contours at initialization (bottom).

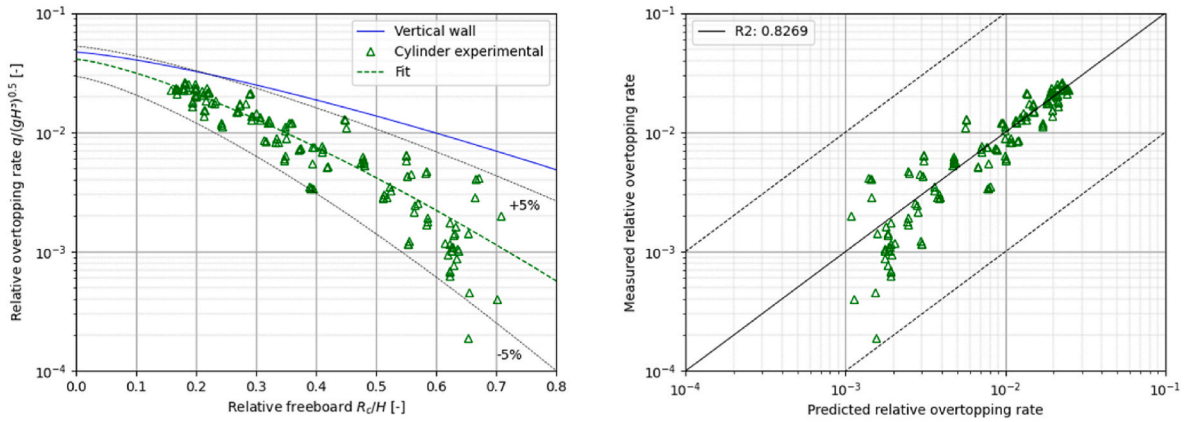

Fig. 8. Measured relative overtopping discharge with 5% under and upper exceedance limits (left). Comparison of the measured and predicted relative overtopping discharges (right). Three diagonal lines indicate the conditions that the prediction is 10 times, equal to, and 0.1 times the measured rate.

$1{\cdot}10^{-4}$ m^2/s^3 respectively. In addition, the Durbin's realizability constraint has been applied (Durbin, 1996) in order to avoid a possible artificial growth of the eddy viscosity in the free surface (Larsen and Fuhrman, 2018), (Mayer and Madsen, 2000). Only one half of the flume has been simulated by establishing the symmetry plane of the domain.

For the sake of simplicity, in the simulations where the water collecting structure is included, the motion of accumulated water inside the tank is not simulated, but it is left free to flow out of the computational domain, because overtopped water amount is computed at the vertical transversal plane located at the centre of the cylinder and over its crest in the two type of simulations.

3.2.3. Mesh

The computational mesh consists of prismatic hexahedral cells. The total number of cells varies between $9.5{\cdot}10^5$ and $2.5{\cdot}10^6$, depending on the simulated case. Fig. 6 shows the local mesh refinement at the free surface and around the cylinder. Free surface refinement consists of cells that are longer in wave propagation direction than in the vertical direction with an aspect ratio of 2 including 20 cells per wave height.

In the damping zone upstream from the outlet section the mesh is coarsened because there is no need of such a fine resolution. Moreover, having a bigger cell size improves damping effect as it increases numerical dissipation (Windt et al., 2019). This final mesh configuration has been the result of an iterative process until the solution has led to unchanged results independent on the mesh. The time step size separating two consecutive time iterations has been selected low enough to fulfil the Courant-Friedrichs-Lewy condition by taking into account the magnitude of the cells and the celerity of the wave. A maximum Courant number of 0.33 has been allowed. This fact, together with a 2nd order temporal discretization, produces a sharp interface between the two phases and prevents the appearance of smearing effects due to numerical diffusion.

3.2.4. Initial conditions

Fig. 7 shows the initial free surface position, fluid velocity and pressure fields calculated with eqs. (20)–(22), i.e higher Stokes wave theory. The damping region is considered from the beginning and the free surface position is initialized such that the cylinder position is next to a wave trough, which helps the solution to converge faster during the first iterations.

3.2.5. Numerical model tests

Two different numerical test campaigns have been carried out under regular wave conditions. The first campaign studies the wave interaction with the fixed cylinder and the attached collecting structure for the model validation by contrasting with the experimental results. The second campaign studies numerically the wave interaction with the cylinder alone, by following the same validated numerical scheme, to prevent a possible disturbance of the collecting structure on the original phenomenon.

In the validation stage, 15 tests have been chosen from the experimental campaign to be simulated numerically. The consideration of the whole range of relative crest freeboard has been observed in the validation process and, consequently, a wide range of R_c/H between 0.16 and 0.72 has been covered, within the same experimental matrix of wave heights ranging from 0.09 m to 0.14 m, and periods from 0.8 s to 1.3 s (Table 1).

For the second stage, with the cylinder alone, the numerical tests have been carried out with the selected wave periods and heights with four different crest freeboard values: R_c = 20 mm, 40 mm, 65 mm, 90 mm. In addition, two different cylinder diameters of D = 110 mm and 82.5 mm have been analysed to check the independence of the general dimensionless tendency from the cylinder diameter.

The evolution of the free surface elevation with time is computed by computational gauges representing R1, R2 and R3 of the experiment, in order to check the characteristics of the imposed computational wave. Another computational gauge is placed on top of the cylinder in the same way as R4, to compute the flow thickness on top of the cylinder. The evolution of the overtopping mass flow with time is computed at the vertical transversal rectangular section on top of the cylinder.

The mean overtopping discharge, q, is determined by integrating the overtopping mass flow rate to get the total overtopped volume and dividing it by the duration of the test and the cylinder diameter (25).

$$q = \frac{\frac{1}{\rho}\cdot\int_0^{t_o}\dot{m}_o\,dt}{t_o\cdot D} \tag{25}$$

where ρ stands for density, $\dot{m}_o$ is the water mass flow at the crest of the cylinder, t_o is the total test duration and D is the cylinder diameter. The value is nondimensionalized with respect to wave height to get the relative overtopping discharge ($q/(gH^3)^{0.5}$).

4. Results and discussion

4.1. Relative overtopping rate

In this section the experimental and numerical data will be fitted to analytical tendencies for both the validation and the definition stages to characterize the overtopping behaviour of a fixed cylinder. Because the cylinder is not affected by an influencing foreshore and a non-impulsive regime has been confirmed, the relative overtopping rate can be estimated with a Weibull-type expression (Eq. (1)).

As expected in this type of tests, the scatter in the data for both the experimental measurements and the numerically predicted rates is

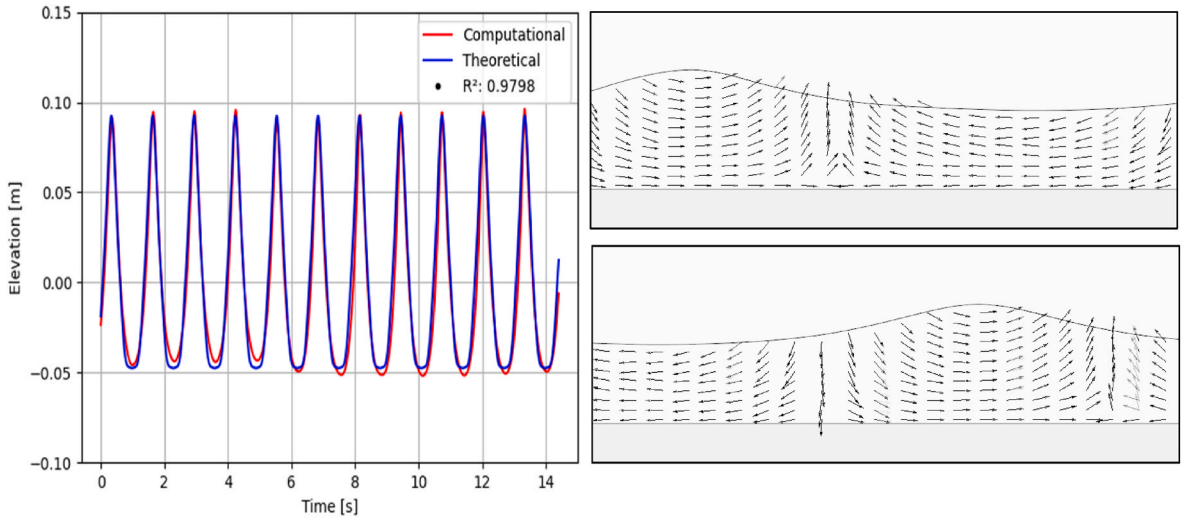

Fig. 9. Computed time series of surface elevations in the simulation of a periodic wave train (blank run: H = 0.14 m, T = 1.3 s, h = 0.3 m) and orbital velocity snapshots of two consecutive wave crests on the symmetry plane after 10 periods.

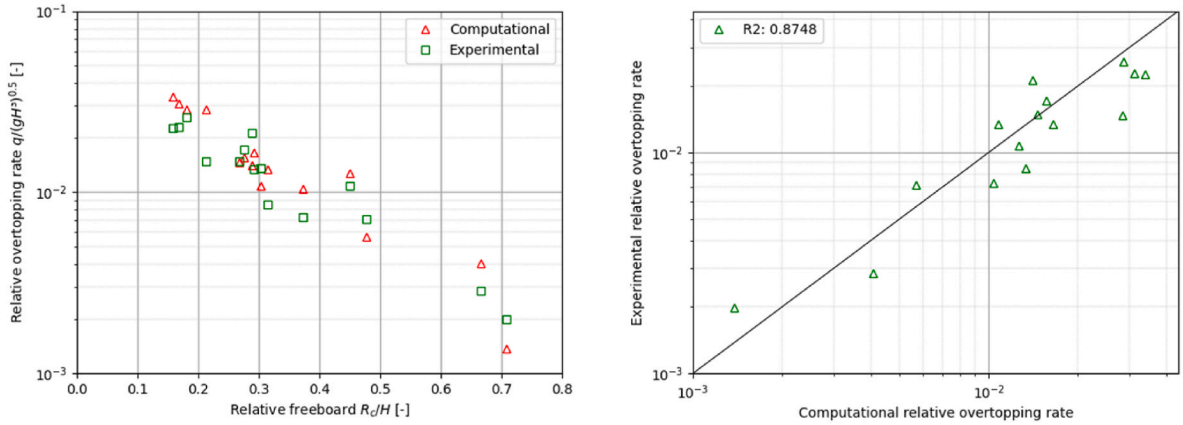

Fig. 10. Comparison between experimentally measured (green squares) and numerically obtained (red triangles) relative overtopping rate (left). Comparison of the experimental and computational relative overtopping discharges (right).

significant, which means that the dispersion of the fitting process needs to be quantified to evaluate the performance of the fitted expression. Here, the probabilistic approach presented in (van der Meer et al., 2018) has been used. After the fitting process, the covariance matrix of the fitting parameters has been used in order to get the standard deviation of each stochastic parameter. Assuming the error to be normally distributed, the 5% exceedance lines have been calculated as $a_i + 1.64\sigma$ and $a_i - 1.64\sigma$, being a_i the mean value of the ith fitting parameter and σ its standard deviation.

The results are compared with the analogous expression valid for linear vertical walls.

4.1.1. Experimental results

Fig. 8 shows the evolution of the experimental relative overtopping discharge $q/(gH^3)^{0.5}$ as a function of the relative freeboard R_c/H together with the evaluation of the dispersion of the data.

The experimental results of the fixed vertical cylinder (green triangles) follow a similar tendency to the curve characteristic of the vertical wall with no influencing foreshore under non-impulsive conditions (top blue line). However, the relative overtopping discharge in the vertical cylinder decreases more pronouncedly with the increase of the relative freeboard than in the case of vertical walls.

Following the same empirical approach as for overtopping over vertical seawalls under extreme sea conditions, the group of points has been fitted by a non-linear least square fitting routine with the analytical equation (1) by using constants a, b and c as fitting parameters. The resulting equation is very similar to equation (3) corresponding to vertical walls but accounting for the lower effective discharge:

$$\frac{Q}{\sqrt{gH^3D}} = 0.0406 \cdot \exp\left[-\left(3.70\frac{R_c}{H}\right)^{1.34}\right] \tag{26}$$

The 5% under and upper exceedance limits (90% confidence band) are displayed. Almost all the data are contained in the 90%-confidence band indicating the extent of the representativeness of the analytical expression regarding the collection of experimental points.

The goodness of this fit has been characterised by the coefficient of determination, R^2, which is calculated as the square of the correlation coefficient between measured and predicted data. In this case the coefficient takes a value of $R^2 = 0.8329$. In addition to the prediction, there are added two dotted diagonals corresponding to the prediction being 10 times and 0.1 times the measured data. Fig. 8 shows how the experimental dispersion grows for higher freeboards but without abandoning this band.

4.1.2. Validation of the numerical model

The stability of the waves during the simulation time has been confirmed in the numerical flume. Fig. 9 shows a good correlation

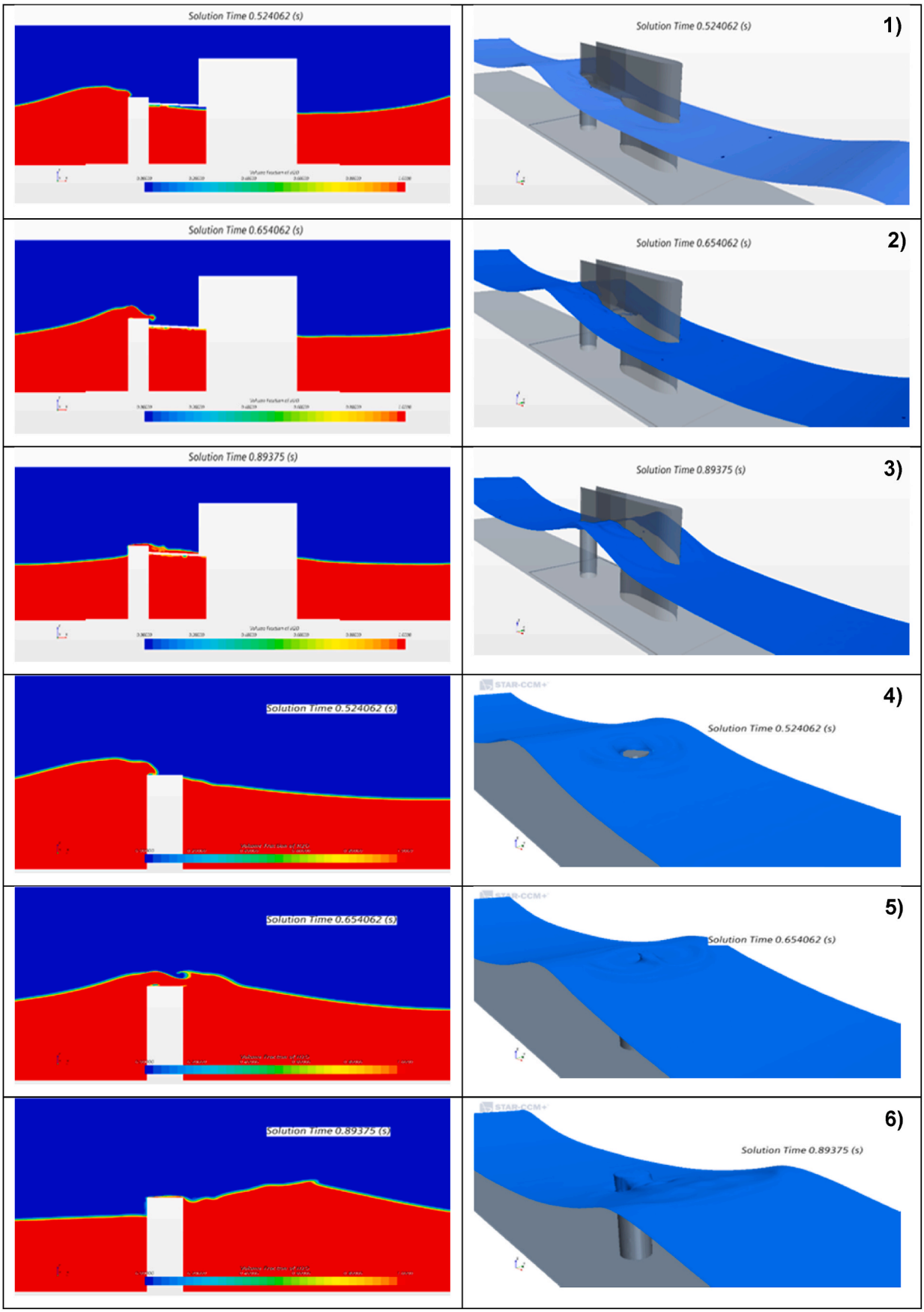

Fig. 11. Example of simulated overtopping event: volume fraction of water at the symmetry plane (left), representation of the free surface (right) corresponding to the computational test H = 0.14 m, T = 1.3 s, h = 0.3 m, Rc = 0.04 m. (1–3) With collecting tank, (4–6) without collecting tank.

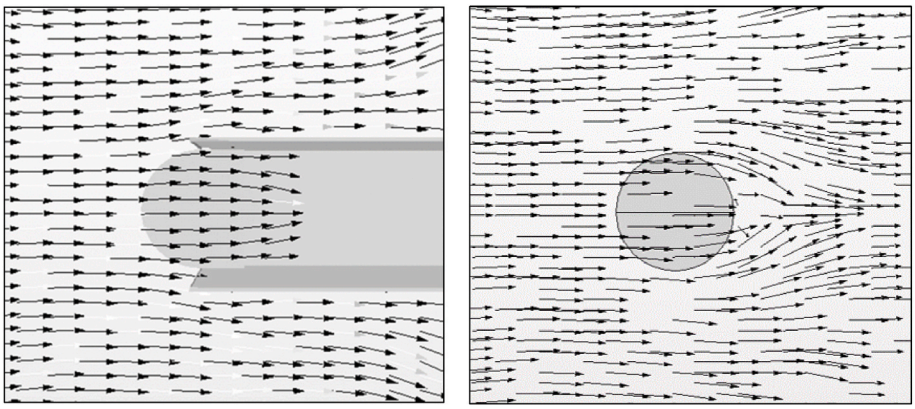

Fig. 12. Vector field of the free surface for a wave crest going past the cylinder with (left) and without (right) the collecting structure. Test: H = 0.14 m, T = 1.3 s, h = 0.3 m, Rc = 0.04 m.

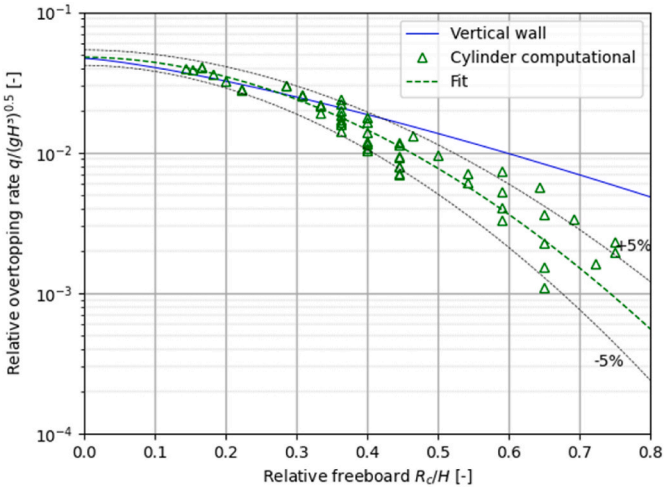

Fig. 13. Computational relative overtopping rate.

between the simulated wave and the theoretical one with a steady wave height. In addition, the orbital velocity vector field reports a configuration congruent with the undisturbed potential flow of the wave.

The values of relative overtopping discharge measured in the experimental tests have been compared to the ones obtained by the numerical model. In the validation stage of the numerical model the collecting structure has been included in the simulation setup, because a certain influence of the interaction of the waves with the back solid structure of the chute and collecting tank on the overtopping volume over the front cylinder may be expected in advance. This hypothesis is confirmed in a next subsection when comparing the results obtained with and without the structure.

Fig. 10 shows the comparison of the numerical tests and their corresponding experimental measurements performed under the same wave conditions. Singular tests all along the experimental freeboard range from 0.14 to 1 have been selected for the validation of the computational model. It can be noticed that the trends of both the numerical and experimental values are very similar, entailing a good prediction by the numerical model of the behaviour of relative overtopping discharge over the structure. Although some discrepancies are observed, a good determination factor of $R^2 = 0.8748$ has been obtained for the correlation between experimental and computational results. The computational model predicts no overtopping discharge for freeboard values of 0.8 and greater, in the same way as in the experimental campaign.

The source of discrepancies between individual results may come from the difference between the experimental and numerical reflection dissipation system or between the numerical and experimental approaches used for wave generation.

4.1.3. Computational results

Once the model has been validated, the same numerical setup (i.e. governing equations, mesh, boundary and initial conditions and numerical scheme) is applied to characterize the overtopping discharge over the cylinder alone, without the presence of an interfering collecting structure.

Fig. 11 shows one representative example of a simulated overtopping event, with and without the presence of the collecting structure, where an individual wave is travelling from the left to the right and interacts with the vertical cylinder. From the analysis of the images, the overtopping process is confirmed to be non-impulsive since no violent wave breaking takes place against the structure or in its vicinity, and the overtopped volume takes place in the form of a continuous green water layer flowing over the crest of the cylinder and no aerated fast water jet has been detected so far. The flow pattern of the overtopped flow is different when comparing the case with the collecting tank (snapshots 1–3) and without the collecting tank (snapshots 4–6) because in the second case the downstream part of the wave at the back of the cylinder affects the overtopping process, whereas in the first case the vertical walls of the chute conduce the overtopped water layer without lateral influence of the propagating wave.

Fig. 12 shows the velocity vector field at the free surface of the wave crest when passing the cylinder in the two different cases being analysed. The influence of the collecting structure on the flow field is noticeable again.

In the case with collecting structure (Fig. 12 left) it can be observed clearly the influence of the vertical walls of the chute directing the water overtopped flow to the collecting tank, while the outside region of the wave crest progresses parallel to those vertical walls. In contrast to the previous case, when the cylinder is simulated alone (Fig. 12 right) the velocity vectors can turn around the cylinder provoking an additional lateral and downstream influence on the main central overtopped flow over the cylinder. This is the reason why the computational data coming from the case with the cylinder alone have been taken as a reference, whereas the case with collecting structure has been used only for the numerical model validation purposes.

Fig. 13 shows the results of the computational model corresponding to a fixed vertical cylinder alone (green triangles), together with the curve corresponding to a vertical wall with no influencing foreshore (blue). In the same way as in the experimental case, a similar tendency is observed for a solitary vertical cylinder in comparison to a vertical wall, but progressively departing downwards because of a markedly smaller relative overtopping discharge the higher the relative freeboard is

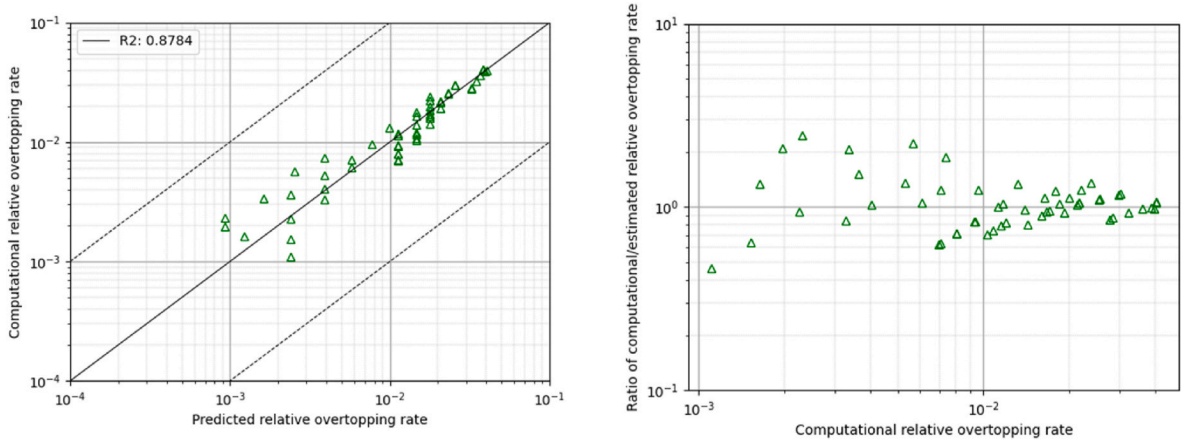

Fig. 14. Correlation between computational and estimated results (left). Ratio of the computed to the estimated overtopping rate (right).

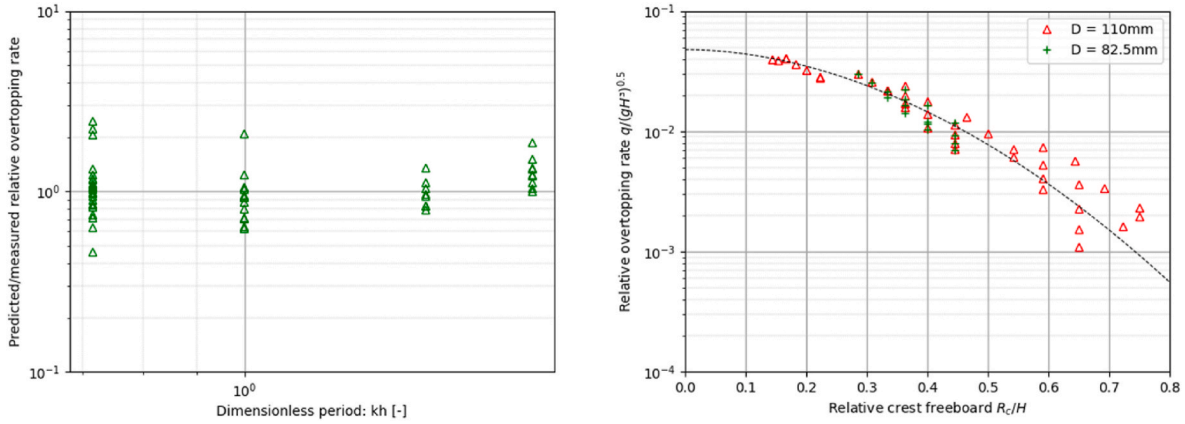

Fig. 15. Ratio of the dimensionless predicted to the measured overtopping vs the dimensionless period (left). Relative overtopping rate vs relative crest freeboard highlighting different diameters (right).

considered.

The collection of data has been fitted to the model represented by equation (1) resulting in:

$$\frac{Q}{\sqrt{gH^3D}} = 0.0478 \cdot \exp\left[-\left(2.74\,\frac{R_c}{H}\right)^{1.9}\right] \tag{27}$$

The majority of the computational data falls within the 90% confidence band indicating the good representativeness of the analytical expression.

In equation (27) the pre-exponential constant of the vertical cylinder is very similar to the corresponding value in equation (3) of vertical walls, revealing that there is no relevant difference for the overtopping discharge under zero freeboard conditions or for very low values of the relative freeboard. The general prediction of relative overtopping rate in a vertical wall with no influencing foreshore and a vertical cylinder is very similar up to a value of $R_c/H = 0.3$.

However, parameters b and c, which determine the curvature of the model, are higher in the case of a vertical cylinder than in the case of a vertical wall leading to a more pronounced decrease of the mean overtopping discharge as the relative crest freeboard increases, as it has been observed graphically.

High values of relative freeboard show an increase in the dispersion of the data in the same way as in the experimental case, which is a typical property of this type of studies (van der Meer et al., 2018; Altomare et al., 2016). Although a higher scatter in the lower discharge region is inherent to the nature of overtopping, the resolution of the computational model also comes into place when analyzing the ability of the model to capture very small overtopping flows. Fig. 14 (left) shows a very good correlation between the computed overtopping rates and the estimation carried out using the fitted model (27).

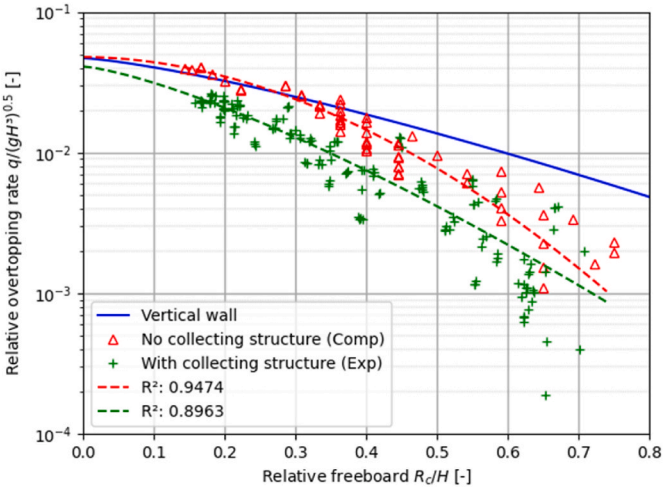

Fig. 16. Relative overtopping discharge with and without collecting structure.

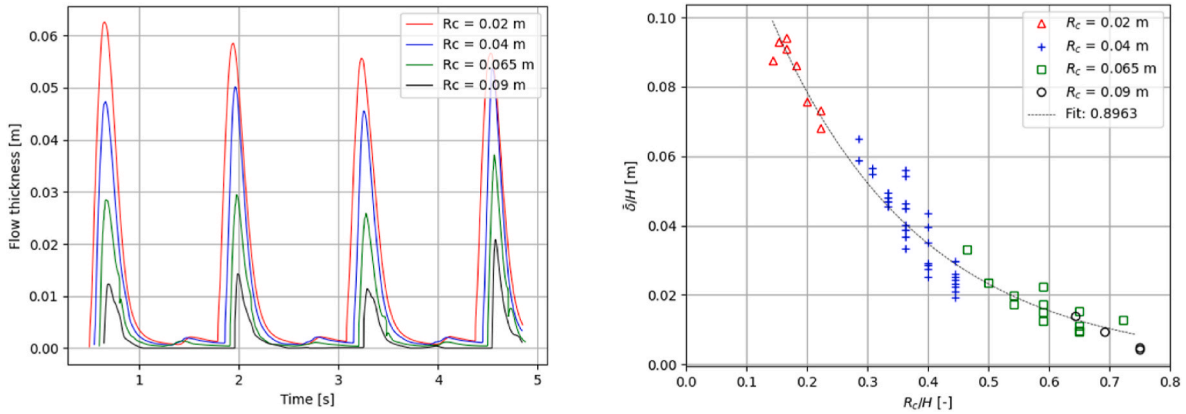

Fig. 17. Computational flow thickness time series with different freeboards under constant wave conditions: H = 0.14m, T = 1.3s, h = 0.3m. (left). Non-dimensionalized mean flow thickness vs relative crest freeboard (right).

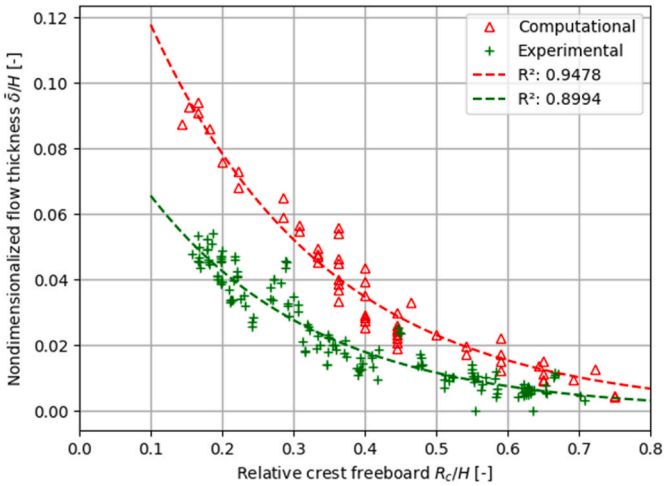

Fig. 18. Comparison between experimental and computational values of non-dimensionalized flow thickness vs relative crest freeboard.

The coefficient of determination takes a value of $R^2 = 0.8784$ and the collection of computational points are very well concentrated along the prediction line inside the band limited by 10 times and 0.1 times the calculated values. Fig. 14 (right) denotes higher dispersion for lower values of the relative overtopping rate but, in addition, a balanced scatter with no bias depending on the magnitude of the overtopping rate.

The possible influence of wave period has also been addressed. In the case of vertical breakwaters and seawalls not subjected to wave breaking, the influence of the period is reported to be very small or non-existent (van der Meer and Bruce, 2014). Fig. 15 (left) shows the ratio between the predicted and the computed relative overtopping rate, plotted against the product of the wavenumber, k, and the water depth, h, which is a measure of the period given in a dimensionless form. According to the data, the influence of the period on the overtopping process is very small. A slight deviation from the horizontal value can be observed for the highest values of the product kh, which correspond to waves with higher steepness being closer to the breaking limit. Nevertheless, no marked tendency is observed for that deviation.

In addition, the influence of the diameter of the cylinder on the dimensionless relationship has been studied. Numerical analysis has been carried out with two different diameters with a common relative freeboard range from 0.28 to 0.44. Fig. 15 (right) shows the numerical results differentiating the collection of values got for each diameter. No significant variation in the computed relative overtopping rate has been observed, as simulations using the same wave characteristics lead to very similar values for both diameters.

Finally, the relative overtopping discharge values obtained using the numerical model applied to the solitary cylinder have been compared to the ones obtained from the experiments in order to study how the collecting structure may affect the overtopping phenomenon (Fig. 16).

Results obtained from the experimental tests with the collecting structure show a similar trend as the ones considering the cylinder alone with the dimensionless overtopping discharge decreasing with

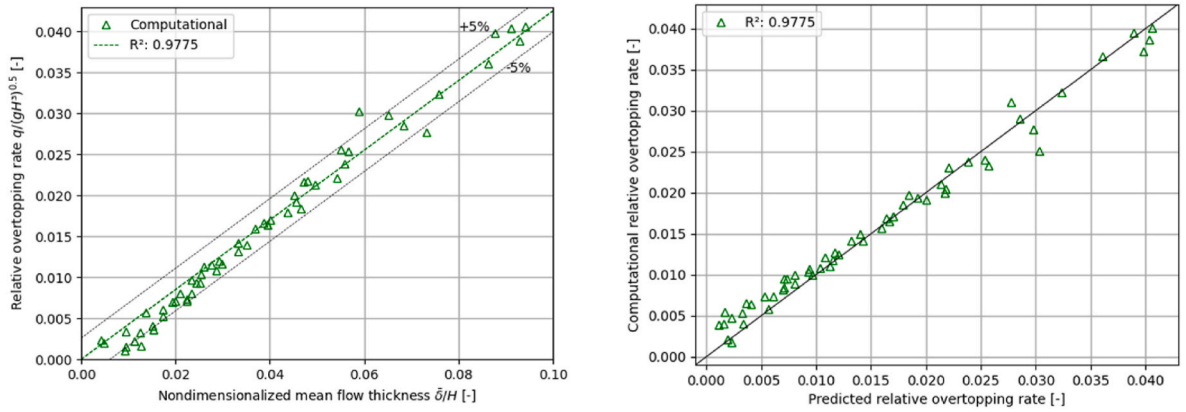

Fig. 19. Comparison of the measured and computed nondimensionalized mean flow thickness with respect to relative crest freeboard.

increasing relative freeboard with a Weibull-shaped function. However, the presence of the collecting structure reduces significantly the overtopping discharge over the cylinder, leading to a difference up to a 45% in the vicinity of $R_c/H = 0.4$. This fact validates the effort of analysing numerically the case of a solitary cylinder by means of a validated CFD model.

4.2. Flow thickness

The time series of flow thickness on top of the cylinder has been measured in each simulation. Although individual overtopping volumes over a fixed cylinder can be computed easily in numerical simulations, an indirect measurement of the overtopping discharge may be very interesting while performing experimental tests or real time measurements, because it could allow to estimate the relative overtopping discharge without the need of a collecting structure. Fig. 17 (left) shows a progressive increase of the flow thickness time series as the freeboard decreases. Moreover, a generalized tendency can be observed when plotting the nondimensionalized average flow thickness $\overline{\delta}/H$, computed with equation (4), with respect of the relative freeboard in Fig. 17 (right).

This tendency of decreasing relative mean flow thickness with larger relative freeboards turns out to be a common behaviour regardless of the magnitude of the individual freeboard. A common exponential correlation has been observed between these two parameters with pre-exponential and exponential coefficients obtained from a fitting routine to the group of computational values in equation (28):

$$\frac{\overline{\delta}}{H} = 0.1769 \cdot exp\left(-4.11\ \frac{R_c}{H}\right) \tag{28}$$

This expression allows to estimate the mean flow thickness if the relative crest freeboard is known in advance.

An analogous tendency has been observed during the experimental campaign (Fig. 18). The resulting overtopping discharge is lower than the one predicted by the computational model, which is coherent with the reduction of the relative overtopping rate observed in the experiments due to the presence of the collecting structure. Although the specific analytical equation representing the tendency of the experimental points does not have a significant interest because of the influence of the collecting system, it is worth noticing that a similar exponential tendency has been obtained experimentally, which supports the validity of the dependency established from the results of the computational campaign without such a disturbance.

Because the relative crest freeboard is a nondimensional parameter determining both the value of the mean relative overtopping discharge and the mean relative flow thickness, a logical consequence is the capability of the relative mean flow thickness to derive the value of the relative overtopping discharge. This outcome is of great importance because allows the definition of the overtopping discharge from the measurement of the flow thickness and the evaluation of the wave height. Fig. 19 shows this direct relationship with a very good correlation between the two non-dimensional variables. The increase of the relative overtopping rate shows a linear relationship with the non-dimensionalized mean flow thickness defined by (29).

$$\frac{q}{\sqrt{gH^3}} = 0.4252\frac{\overline{\delta}}{H} \tag{29}$$

The majority of the computational data falls within the 90% confidence band indicating the good representativeness of the analytical expression. In addition the coefficient of determination takes a value of $R^2 = 0.9775$ and the collection of computational points are very well concentrated along the prediction line (Fig. 19 - right).

5. Conclusions

In the present study, the parametric dependence of wave overtopping over a fixed vertical cylinder has been studied. For that purpose, a RANS-VOF based numerical model has been developed and implemented using computational fluid dynamic techniques. The numerical model has been validated by contrasting the overtopping results with the ones obtained in a physical model tested in the wave flume of the Energy Engineering Department at UPV/EHU. The overtopping water collecting structure used in the experimental campaign has come out to affect significantly the overtopping process over the structure being analysed. Consequently, once the numerical model has been validated, it has been used to describe the process without the presence of the collecting structure in a wide range of wave periods, wave heights, freeboards and different cylinder diameters.

As a result of the analysis a dimensionless relationship of Weibull type has been derived to predict the relative mean overtopping discharge in a fixed vertical cylinder as a function of the relative freeboard, as the main conclusion of this piece of research. This specific empirical formula has been compared with the predictive formula established for linear vertical walls in analogous non-impulsive wave conditions.

Finally, a dimensionless relationship has been proposed to derive the relative mean overtopping discharge from the indirect value of the flow thickness measured at the centre of the circular crest of the cylinder. This correlation may constitute a useful indirect methodology to experimentally evaluate the overtopping discharge in a full-scale cylindrical prototype.

CRediT authorship contribution statement

G.A. Esteban: Conceptualization, Methodology, Investigation, Writing – review & editing, discussed the results and contributed to the final manuscript. **A. Aristondo:** Investigation, Software, Data curation, and, Writing – original draft, Formal analysis, and, Supervision, the results and contributed to the final manuscript. **U. Izquierdo:** Conceptualization, Methodology, Writing – review & editing, discussed the results and contributed to the final manuscript. **J.M. Blanco:** Conceptualization, Formal analysis, and, Supervision, Project administration, and, Funding acquisition, discussed the results and contributed to the final manuscript. **G. Pérez-Morán:** Project administration, and, Funding acquisition, discussed the results and contributed to the final manuscript..

Declaration of competing interest

The authors declare that they have no known competing financial interests or personal relationships that could have appeared to influence the work reported in this paper.

Acknowledgements

The study was conducted within the framework of the research project MATHEO (KK-2019/00085) funded by the Basque Government. The authors would like also to express their gratitude for the support provided by the Research Groups of the UPV/EHU (GIU19/029) and the Basque Government (IT1314-19), as well as the support provided by the Joint Research Laboratory on Offshore Renewable Energy (JRL-ORE). Open Access funding provided by University of Basque Country.

Nomenclature

c	Wave celerity
$C_{\varepsilon 1}$, $C_{\varepsilon 2}$, C_{μ}	Closure coefficients for the turbulent dissipation rate and turbulent kinetic energy transport equations
D	Diameter of the cylinder
F_i	ith component of the external field force per unit mass
g	Acceleration of gravity
h	Water depth
h*	Impulsiveness parameter
H	Wave height
H_{m0}	Significant wave height
k	Wave number
k_t	Turbulent kinetic energy
$L_{m-1,0}$	Deep water wave length corresponding to the mean energy wave period $T_{m-1,0}$ for deep waves
m_1	Wave height to paddle stroke ratio (H/S)
$\dot{m}_o$	Overtopping mass flow rate
p	Pressure
q	Mean overtopping discharge
Q	Mean overtopping flow rate
R^2	Determination factor
R_c	Crest freeboard
s	Wave steepness
S	Stroke length of the piston wavemaker
S_i	source or sink of the ith component of the momentum
S_{ij}	Viscous stress tensor
S_z^d	Resistance term
t	Time
t_o	Time interval of the overtopping event
T	Wave period
$T_{m-1,0}$	Energy wave period calculated as the quotient of the moments m_{-1}/m_0 of the wave energy spectrum
u	Horizontal fluid particle velocity
u'_i	fluctuating velocity component
U_i	ith time-averaged velocity component
Ur	Ursell number
w	Vertical fluid particle velocity
V_o	Overtopped volume
α	Water volume fraction
δ	Flow thickness
$\overline{\delta}$	Average flow thickness
δ_{ij}	Kronecker delta function
ε_t	Turbulent kinetic energy dissipation rate
η	(x,t) Free surface elevation as a function of the length and time
λ	Wave length
μ	Dynamic molecular viscosity
μ_t	Eddy viscosity
ρ	Fluid density
σ	Standard deviation
σ_k, σ_ε	Closure coefficients for the turbulent dissipation rate and turbulent kinetic energy transport equations
φ	Phase angle of the wave
$\varnothing(x,z,t)$	Velocity potential as a function of the length, height and time
ω	Wave frequency

References

Akgul, M.A., Kabdasli, M.S., 2017. Experimental study for the hydraulic efficiency of an overtopping type wave energy converter with a circular runup ramp. Balikesir Üniver. Fen Bilim. Enstitüsü Derg. 19 https://doi.org/10.25092/baunfbed.322406, 118–118.

Altomare, C., Suzuki, T., Chen, X., Verwaest, T., Kortenhaus, A., 2016. Wave overtopping of sea dikes with very shallow foreshores. Coast. Eng. 116, 236–257. https://doi.org/10.1016/j.coastaleng.2016.07.002.

Buccino, M., Daliri, M., Dentale, F., Calabrese, M., 2019a. CFD experiments on a low crested sloping top caisson breakwater. Part 2. Analysis of plume impact. Ocean. Eng. 173, 345–357. https://doi.org/10.1016/j.oceaneng.2018.12.065.

Buccino, M., Daliri, M., Dentale, F., Di Leo, A., Calabrese, M., 2019b. CFD experiments on a low crested sloping top caisson breakwater. Part 1. nature of loadings and global stability. Ocean. Eng. 182, 259–282. https://doi.org/10.1016/j.oceaneng.2019.04.017.

Chakrabarti, S.K., 1994. Offshore Structure Modeling, Applied Ocean Research, Advanced Series on Ocean Engineering. WORLD SCIENTIFIC. https://doi.org/10.1142/2127.

Chen, X., Hofland, B., Altomare, C., Suzuki, T., Uijttewaal, W., 2015. Forces on a vertical wall on a dike crest due to overtopping flow. Coast. Eng. 95, 94–104. https://doi.org/10.1016/j.coastaleng.2014.10.002.

Chen, W., Warmink, J.J., van Gent, M.R.A., Hulscher, S.J.M.H., 2021. Numerical modelling of wave overtopping at dikes using OpenFOAM. Coast. Eng. 166 https://doi.org/10.1016/j.coastaleng.2021.103890.

Choi, J., Yoon, S.B., 2009. Numerical simulations using momentum source wave-maker applied to RANS equation model. Coast. Eng. 56, 1043–1060. https://doi.org/10.1016/j.coastaleng.2009.06.009.

Contestabile, P., Crispino, G., Di Lauro, E., Ferrante, V., Gisonni, C., Vicinanza, D., 2020. Overtopping breakwater for wave Energy Conversion: review of state of art, recent

advancements and what lies ahead. Renew. Energy 147, 705–718. https://doi.org/10.1016/j.renene.2019.08.115.
Dalrymple, R.A., Knio, O.M., Cox, D.T., Gesteira, M., 2002. Using a Lagrangian particle method for deck overtopping. In: Fourth International Symposium on Ocean Wave Measurement and Analysis, pp. 1082–1091. https://doi.org/10.1061/40604(273)110.
Dang, B.L., Nguyen-Xuan, H., Abdel Wahab, M., 2021. Numerical study on wave forces and overtopping over various seawall structures using advanced SPH-based method. Eng. Struct. 226, 111349. https://doi.org/10.1016/j.engstruct.2020.111349.
Di Lauro, E., Lara, J.L., Maza, M., Losada, I.J., Contestabile, P., Vicinanza, D., 2019. Stability analysis of a non-conventional breakwater for wave energy conversion. Coast. Eng. 145, 36–52. https://doi.org/10.1016/j.coastaleng.2018.12.008.
Di Lauro, E., Maza, M., Lara, J.L., Losada, I.J., Contestabile, P., Vicinanza, D., 2020. Advantages of an innovative vertical breakwater with an overtopping wave energy converter. Coast. Eng. 159, 103713. https://doi.org/10.1016/j.coastaleng.2020.103713.
Durbin, P.A., 1996. On the k-3 stagnation point anomaly. Int. J. Heat Fluid Flow 17, 89–90. https://doi.org/10.1016/0142-727X(95)00073-Y.
Fenton, J.D., 1985. A fifth-order Stokes theory for steady waves. J. Waterw. Port, Coast. Ocean Eng. 111, 216–234. https://doi.org/10.1061/(ASCE)0733-950X, 1985)111:2(216.
Galván, J., 2018. NAUTILUS-DTU 10MW floating offshore wind turbine at gulf of Maine. In: WindEurope. Hamburg.
Gómez-Gesteira, M., Cerqueiro, D., Crespo, C., Dalrymple, R.A., 2005. Green water overtopping analyzed with a SPH model. Ocean. Eng. 32, 223–238. https://doi.org/10.1016/j.oceaneng.2004.08.003.
Han, Z., Liu, Z., Shi, H., 2018. Numerical study on overtopping performance of a multi-level breakwater for wave energy conversion. Ocean. Eng. 150, 94–101. https://doi.org/10.1016/j.oceaneng.2017.12.058.
Hasselmann, K., Barnett, T.P., Bouws, E., Carlson, D.E., Cartwright, D.E., Enke, K., Ewing, J.A., Glenapp, H., Hasselmann, D.E., Kruseman, P., Meerburg, A., Müller, P., Olbers, D.J., Richter, K., Sell, W., Walden, H., 1973. Measurements of wind wave growth and swell decay during the Joint north sea wave project (JONSWAP). Dtsch. Hydrogr. Zeitschrift 8, 1–95.
Hirt, C., Nichols, B., 1981. Volume of fluid (VOF) method for the dynamics of free boundaries. J. Comput. Phys. 39, 201–225. https://doi.org/10.1016/0021-9991(81)90145-5.
Hughes, S.A., 1993. Physical Models and Laboratory Techniques in Coastal Engineering, Advanced Series on Ocean Engineering. WORLD SCIENTIFIC. https://doi.org/10.1142/2154.
Isaacson, M., 1991. Measurement of regular wave reflection. J. Waterw. Port, Coast. Ocean Eng. 553–569.
Izquierdo, U., Esteban, G.A., Blanco, J.M., Albaina, I., Peña, A., 2019. Experimental validation of a CFD model using a narrow wave flume. Appl. Ocean Res. 86, 1–12. https://doi.org/10.1016/j.apor.2019.02.012.
Izquierdo, U., Galera-Calero, L., Albaina, I., Vázquez, A., Esteban, G.A., Blanco, J.M., 2021. Experimental and numerical determination of the optimum configuration of a parabolic wave extinction system for flumes. Ocean. Eng. 238, 1–11.
Jonkman, J., 2010. Definition of the Floating System for Phase IV of OC3. Colorado.
Larsen, B.E., Fuhrman, D.R., 2018. On the over-production of turbulence beneath surface waves in Reynolds-averaged Navier-Stokes models. J. Fluid Mech. 853, 419–460. https://doi.org/10.1017/jfm.2018.577.
Lashley, C.H., Zanuttigh, B., Bricker, J.D., van der Meer, J., Altomare, C., Suzuki, T., Roeber, V., Oosterlo, P., 2020. Benchmarking of numerical models for wave overtopping at dikes with shallow mildly sloping foreshores: accuracy versus speed. Environ. Model. Software 130, 104740. https://doi.org/10.1016/j.envsoft.2020.104740.
Launder, B.E., Sharma, B.I., 1974. Application of the energy-dissipation model of turbulence to the calculation of flow near a spinning disc. Lett. Heat Mass Tran. 1, 131–137. https://doi.org/10.1016/0094-4548(74)90150-7.
Liu, Z., Han, Z., Shi, H., Yang, W., 2018. Experimental study on multi-level overtopping wave energy convertor under regular wave conditions. Int. J. Nav. Archit. Ocean Eng. 10, 651–659. https://doi.org/10.1016/j.ijnaoe.2017.10.004.
Liu, X., Liu, Y., Lin, P., Li, A. jun, 2021. Numerical simulation of wave overtopping above perforated caisson breakwaters. Coast. Eng. 163, 103795. https://doi.org/10.1016/j.coastaleng.2020.103795.
Lu, Y. jin, Liu, H., Wu, W., Zhang, J. shan, 2007. Numerical simulation of two-dimensional overtopping against seawalls armored with artificial units in regular waves. J. Hydrodyn. 19, 322–329. https://doi.org/10.1016/S1001-6058(07)60065-1.
Mansard, E.P.D., Funke, E.R., 1980. The measurement of incident and reflected spectra using a least squares method. 17th Int. Conf. Coast. Eng. 154–172.
Mayer, S., Madsen, P.A., 2000. Simulation of breaking waves in the surf zone using a Navier-Stokes solver. Coast. Eng. 2000 - Proc. 27th Int. Conf. Coast. Eng. ICCE 276, 928–941. https://doi.org/10.1061/40549(276)72, 2000.
Musa, M.A., Maliki, A.Y., Ahmad, M.F., Sani, W.N., Yaakob, O., Samo, K.B., 2017. Numerical simulation of wave flow over the overtopping breakwater for energy conversion (OBREC) device. In: Procedia Engineering. Elsevier Ltd, pp. 166–173. https://doi.org/10.1016/j.proeng.2017.08.131.
National Instruments, 2018. LabVIEW 18.0f2 (64-bit).
Nørgaard, J.Q.H., Lykke Andersen, T., Burcharth, H.F., 2014. Distribution of individual wave overtopping volumes in shallow water wave conditions. Coast. Eng. 83, 15–23. https://doi.org/10.1016/j.coastaleng.2013.09.003.
Pearson, J., Bruce, T., Allsop, W., 2001. Prediction of wave overtopping at steep seawalls - variabilities and uncertainties. In: Proceedings of the International Symposium on Ocean Wave Measurement and Analysis, pp. 1797–1808. https://doi.org/10.1061/40604(273)181.
Perić, R., Abdel-Maksoud, M., 2016. Reliable damping of free-surface waves in numerical simulations. Ship Technol. Res. 63, 1–13. https://doi.org/10.1080/09377255.2015.1119921.
Pierson, W.J., Moskowitz, L., 1964. A proposed spectral form for fully developed wind seas based on the similarity theory of S. A. Kitaigorodskii. J. Geophys. Res. 69, 5181–5190.
Pillai, K., Etemad-Shahidi, A., Lemckert, C., 2017. Wave overtopping at berm breakwaters: experimental study and development of prediction formula. Coast. Eng. 130, 85–102. https://doi.org/10.1016/j.coastaleng.2017.10.004.
Pullen, T., Allsop, W., Bruce, T., Geeraerts, J., 2003. Violent wave overtopping: CLASH field measurements at Samphire. Hoe. Coast. Struct. 2003 - Proc. Conf. 40733, 469–480. https://doi.org/10.1061/40733(147)39.
Shao, S., Ji, C., Graham, D.I., Reeve, D.E., James, P.W., Chadwick, A.J., 2006. Simulation of wave overtopping by an incompressible SPH model. Coast. Eng. 53, 723–735. https://doi.org/10.1016/j.coastaleng.2006.02.005.
Tuan, T.Q., Verhagen, H.J., Visser, P., Stive, M.J.F., 2006. Wave overwash at low-crested beach barriers. Coast Eng. J. 48, 371–393. https://doi.org/10.1142/S0578563406001453.
Ursell, F., 1953. The long-wave paradox in the theory of gravity waves. Math. Proc. Camb. Phil. Soc. 49, 685–694. https://doi.org/10.1017/S0305004100028887.
van der Meer, J.W., Allsop, N.W.H., Bruce, T., De Rouck, J., Kortenhaus, A., Pullen, T., Schüttrumpf, H., Troch, P., Zanuttigh, B., 2018. EurOtop 2018. Manual on Wave Overtopping of Sea Defences and Related Structures. An Overtopping Manual Largely Based on European Research, but for Worldwide Application.
van der Meer, J., Bruce, T., 2014. New physical insights and design formulas on wave overtopping at sloping and vertical structures. J. Waterw. Port, Coast. Ocean Eng. 140, 04014025 https://doi.org/10.1061/(asce)ww.1943-5460.0000221.
van der Meer, J.W., Verhaeghe, H., Steendam, G.J., 2009. The new wave overtopping database for coastal structures. Coast. Eng. 56, 108–120. https://doi.org/10.1016/j.coastaleng.2008.03.012.
van Gent, M.R.A., van den Boogaard, H.F.P., Pozueta, B., Medina, J.R., 2007. Neural network modelling of wave overtopping at coastal structures. Coast. Eng. 54, 586–593. https://doi.org/10.1016/j.coastaleng.2006.12.001.
Vanneste, D.F.A., Altomare, C., Suzuki, T., Troch, P., Verwaest, T., 2014. Comparison of numerical models for wave overtopping and impact on a sea wall. Coast. Eng. Proc. 1, 5. https://doi.org/10.9753/icce.v34.structures.5.
Vázquez, M., Negro, V., López-Gutiérrez, J.S., Monsó, J.L., 2016. Evaluation of wave loads on a new type of perforated caisson. Proc. Inst. Civ. Eng. Marit. Eng. 169, 124–139. https://doi.org/10.1680/jmaen.2015.1.
Victor, L., van der Meer, J.W., Troch, P., 2012. Probability distribution of individual wave overtopping volumes for smooth impermeable steep slopes with low crest freeboards. Coast. Eng. 64, 87–101. https://doi.org/10.1016/j.coastaleng.2012.01.003.
Viriyakijja, K., Chinnarasri, C., 2015. Wave flume measurement using image analysis. Aquat. Procedia 4, 522–531. https://doi.org/10.1016/j.aqpro.2015.02.068.
Williams, H.E., Briganti, R., Romano, A., Dodd, N., 2019. Experimental analysis of wave overtopping: a new small scale laboratory dataset for the assessment of uncertainty for smooth sloped and vertical coastal structures. J. Mar. Sci. Eng. 7, 1–18. https://doi.org/10.3390/jmse7070217.
Windt, C., Davidson, J., Schmitt, P., Ringwood, J.V., 2019. On the assessment of numerical wave makers in CFD simulations. J. Mar. Sci. Eng. 7 https://doi.org/10.3390/JMSE7020047.
Zeidler, R.B., Szmytkiewicz, M., Kolodko, J., Skaja, M., Jednachowski, R., 1994. Wave runup on smooth and rock slopes of coastal structures. J. Waterw. Port, Coast. Ocean Eng. 120, 510–513. https://doi.org/10.1061/(ASCE)0733-950X, 1994)120:5(510.
Zhang, X., Draper, S., Wolgamot, H., Zhao, W., Cheng, L., 2019. Eliciting features of 2D greenwater overtopping of a fixed box using modified dam break models. Appl. Ocean Res. 84, 74–91. https://doi.org/10.1016/j.apor.2019.01.006.